sciendo

Bio-Algorithms and Med-Systems 2022; 18(1): 107-119

Research article

Andrea Gonzalez-Montoro, Julio Barbera, David Sanchez, Alvaro Mondejar, Marta Freire, Karel Diaz, Alejandro Lucero, Santiago Jimenez-Serrano, Jorge Alamo, Constantino Morera-Ballester, John Barrio, Neus Cucarella, Victor Ilisie, Laura Moliner, Celia Valladares, Antonio J. Gonzalez, John Prior and Jose M. Benlloch*

A new brain dedicated PET scanner with 4D detector information

https://doi.org/10.2478/bioal-2022-0083
Received September 20, 2022; accepted December 05, 2022; published online December 19, 2022.

Keywords: Positron Emission Tomography (PET), brain PET, organ-specific PET, Depth-of-Interaction (DOI), Time-of-flight (TOF), semi-monolithic scintillator, Silicon Photomultiplier (SiPM), Application-specific-integrated-circuit (ASIC).

Abstract: In this article, we present the geometrical design and preliminary results of a high sensitivity organ-specific Positron Emission Tomography (PET) system dedicated to the study of the human brain. The system, called 4D-PET, will allow accurate imaging of brain studies due to its expected high sensitivity, high 3D spatial resolution and, by including precise photon time of flight (TOF) information, a boosted signal-to-noise ratio (SNR).

The 4D-PET system incorporates an innovative detector design based on crystal slabs (semi-monolithic) that enables accurate 3D photon impact positioning (including photon Depth of Interaction (DOI) measurement), while providing a precise determination of the photon arrival time to the detector. The detector includes a novel readout system that reduces the number of detector signals in a ratio of 4:1 thus, alleviating comp-lexity and cost. The analog output signals are fed to the TOFPET2 ASIC (PETsys) for scalability purposes.

The present manuscript reports the evaluation of the 4D-PET detector, achieving best values 3D resolution values of <1.6 mm (pixelated axis), 2.7±0.5 mm (monolithic axis) and 3.4±1.1 (DOI axis) mm; 359 ± 7 ps coincidence time resolution (CTR); 10.2±1.5 % energy resolution; and sensitivity of 16.2% at the center of the scanner (simulated). Moreover, a comprehensive description of the 4D-PET architecture (that includes 320 detectors), some pictures of its mechanical assembly, and simulations on the expected image quality are provided.

Introduction

Positron Emission Tomography (PET) constitutes the molecular imaging technique of excellence and is widely used for the diagnose and treatment monitoring of several diseases. Among its several applications, PET imaging is used for understanding the pharmacological treatment of neurological illness and, has helped developing the most recent generation of effective drugs [1]. However, the utility of whole-body (WB-)PET for the clinical diagnosis of mental disorders is still restricted by the complexity of the infrastructure required to generate radiopharmaceuticals and, the significant high cost, limited sensitivity, and resolution of commercially available PET scanners [2].

Organ-specific PET design, which are dedicated to the study of one organ or area in particular, are a promising solution to overcome the previously mentioned limitations of WB-PET [3]. Dedicated PET systems, aim to increase sensitivity (both clinical and

***Corresponding author: Prof. Jose M. Benlloch**, Instituto de Instrumentación para Imagen Molecular (i3M), Centro mixto CSIC – Universitat Politècnica de València, Instituto i3M - UPV, Edificio 8B, 46022, Valencia, Spain. Phone: +34 963879907. Email: benlloch@i3m.upv.es

Andrea Gonzalez-Montoro, David Sanchez, Marta Freire, Alejandro Lucero, Santiago Jimenez-Serrano, John Barrio, Neus Cucarella, Victor Ilisie, Laura Moliner, Celia Valladares and Antonio J. Gonzalez, Instituto de Instrumentación para Imagen Molecular (i3M), Centro mixto CSIC – Universitat Politècnica de València, 46022, Valencia, Spain.

Julio Barbera, Alvaro Mondejar, Karel Diaz, Jorge Alamo and Constantino Morera-Ballester, Oncovision, S. A. - Jeronimo de Monsoriu, 92, 46012, Valencia, Spain.

John Prior, Nuclear Medicine and Molecular Imaging Department, Centre Hospitalier Universitaire Vaudois (CHUV) – Lausanne, Switzerland

physical) as much as possible since they present an optimized geometry to attain the highest possible angular coverage of the organ or area under examination. With physiological healthy parameters varying significantly with age and other conditions, increased sensitivity is critical for early diagnosis and treatment follow up. Moreover, high sensitivity also allows for safer repeated scans for the same patient, decisive for early assessment of treatment progress and in depth physiological and pharmacodynamic occupancy studies. Also, organ-dedicated systems report better performance than standard WB-PET scanners, such as millimetric spatial resolution [4], small footprint and portable designs, higher patient throughput and also, a reduced cost [5]. A drawback of organ-dedicated PET systems is that, these scanners typically focus on the examination of a single organ thus reducing their usage by different areas or departments in a clinical centre.

In the framework of organ-specific imaging scanners, brain dedicated PET systems have demonstrated to be a promising tool for unravelling the insight of the human brain structure as well as providing better diagnose and understanding of several mental conditions [6]. PET application in paediatrics for both study of brain development and its early-age pathologies (learning disabilities, autism, some forms of schizophrenia) has to be a primary goal for these scanners. In this regard, radiation dose is always a key consideration in brain PET [7]. It is interesting that the first PET scanner, proposed by Brownell and Sweet in 1952, was already a dedicated brain PET system [8].

The construction of a high-efficiency brain PET system able to provide such a detailed information, imposes major technological challenges such as novel detector components to reach a spatial resolution in the range of 1-2 mm; handling, storing and processing huge amounts of data or; fast image reconstruction algorithms, among others [9]. In addition, providing accurate reconstructed images within a short time-frame, requires the system to enable Time-of-Flight (TOF) capabilities reducing the statistics needed for precise image reconstruction [10], and, an excellent 3D photon positioning for an homogeneous spatial resolution across the entire field of view (FOV) which demands accurate estimation of the photon depth of interaction (DOI) within the scintillator [11]. Therefore, a detector suitable for brain imaging should present 4D capabilities, being these ones: 3D spatial resolution (x, y, DOI) + TOF capabilities [12] (see also reference [13] for a comprehensive review on the perspectives of brain PET scanners). A 4D detector is feasible now thanks to the last advances in instrumentation [14]. On one hand, current innovation in the development of new scintillating crystals and broad variety of cost-competitive crystals combining significantly higher stopping power, better light yield and on-demand configurable geometry and size are readily available [15-16], making them a very appealing option for the development of brain PET scanners. For example, the introduction of semi-monolithic (slab) scintillators which take advantage of the benefits present in both the pixelated and monolithic crystal configurations [17-18]. On the other hand, the new generation silicon photomultipliers (SiPMs) used for detecting the generated optical photons, have been substantially improved making the photomultiplier tubes (PMT) technology obsolete [19]. They reach a very low dark-count rate, broader detection wave-length spectra, are compatible with magnetic fields thus enabling their simultaneous use with magnetic resonance (MR) systems, provide good timing and spatial resolution and, can be easily adapted to any desired configuration, all this at almost room temperature [20]. Combined, these major improvements translate unprecedented efficiency and flexible configuration detector blocks, very significantly improving clinical performance of next generation organ-specific PET scanners [21]. However, despite gamma ray scintillation detectors have benefited from major breakthroughs during the last decade, these advancements have not been incorporated yet into clinical use for neurological scanners [22].

Trying to exploit these advancements, we are involved in the design and construction of a novel brain PET scanner, called 4D-PET, which is aimed at allowing accurate new studies due to its expected high sensitivity, high 3D spatial resolution and, a signal-to-noise ratio (SNR) boosted by including precise TOF information. We have designed the prototype keeping in mind that the images used by the medical staff, for both diagnosis and observation, are usually a superposition of trans-axial planes, the imprecision of the reconstructed image in the z axis, becomes less manifest. Accounting for this, the given 4D-PET configuration is specifically designed in order to ensure good spatial resolution in the trans-axial plane(s) [23].

The 4D-PET system is based on an innovative detector design constructed using crystal slabs to allow for good 3D photon impact positioning, including photon DOI measurement (critical for dedicated scanners), while providing also a precise determination of the photon arrival time to the detectors. The system is built using 320

detector elements, each composed of an array of 1×16 slab-shaped LYSO elements coupled to a matrix of 8×8 SiPMs. Moreover, the 4D-PET detector electronics includes a novel readout system that reduces the number of output signals in a ratio of 4:1 thus, alleviating system complexity and cost [24]. These output signals are fed to the TOFPET2 ASIC from PETsys [25] for scalability purposes.

The 4D-PET system covers an axial length of 200 mm and has an internal diameter of 280 mm to ensure the coverage of almost completely all the areas of the human brain [26], and with its novel design, will allow the patient to be seated instead of lying down, which is an active, ergonomic and patient-friendly physiological position that may result in improved alignment of brain activity with respect to normal daily life activities. Moreover, the 4D-PET ring head design, frees the patient´s eyesight for active visual stimulation, opening unexplored possibilities for both expanding knowledge of neurophysiological activity and earlier and more accurate diagnosis in multiple pathologies. It should be mentioned that there are other ongoing research and developments aiming at the cost effectiveness of the PET systems as described in references [27-29] as well as on developing complementary methods to the semi-monolithic approach [30].

The present manuscript shows for the first time, a comprehensive description of the 4D-PET architecture, simulations on the expected reconstructed image quality and, pictures of its mechanical assembly. Moreover, the evaluation of the 4D-PET detector in terms of coincidence time resolution (CTR), energy performance and, 3D spatial resolution, are also presented and discussed.

Materials and Methods

This section describes the 4D-PET detector design and the geometry of the full scanner. An explanation of the experimental tests carried out to evaluate the detector performance and, of the simulations performed to assess the image quality of the final system are also provided.

Detector design and evaluation

Aiming to achieve high 3D photon impact positioning, accurate CTR and good energy discrimination, the proposed detector design has been implemented using novel instrumentation technology. Moreover, its dimensions and geometry have been carefully studied to guarantee its scalability for the successful construction of the 4D-Brain PET scanner.

The detector design consists of 1×16 slab-shaped LYSO ($Lu_{1.8}Y_{0.2}SiO_5$: Ce) scintillation elements manufactured by EPIC-crystal Co., Ltd.

The slab geometry is key in our design since it allows to exploit the advantages present in both pixelated and monolithic designs as described in [19], [31], thus, simultaneously enabling good timing resolution and accurate 3D photon impact positioning. On the one hand, the pixelated axis provides sharp and fast signals for accurate timing measurements while providing spatial resolutions as good as the pixel size (<1.6 mm in our design). On the other hand, the monolithic axis allows to retrieve and characterize the scintillation light distribution (LD) shape and enable accurate photon depth of interaction information [32]. Figure 1-left shows a schematic representation of a photon impact in the 1×16 slab-shaped array.

In particular, the scintillation array selected for the construction of the 4D-PET, is composed of 14 rectangular slab-shaped LYSO scintillating crystals of 1.6×24.2×20.0 mm^3, and two wedge-like crystals of similar dimensions (wedge angle of 4.5°), placed on each side. The total dimension of the array is 22.4×25.7 mm^2 (top), 25.7×25.7 mm^2 (bottom), and 20.0 mm thick (see Figure 1-right for a detailed description of the array geometry). The slabs have been polished and specular enhanced reflector (ESR) layers have been placed in between them (for optical isolation), and at the top and lateral sides of the array [33]. The exit face of the scintillator array is coupled by means of optical grease (BC-630, Saint Gobain [34]) to an 8×8 matrix of 3.12×3.12 mm^2 SiPMs (S13360-3075PE with a pixel pitch of 75 µm) from Hamamatsu Photonics [35].

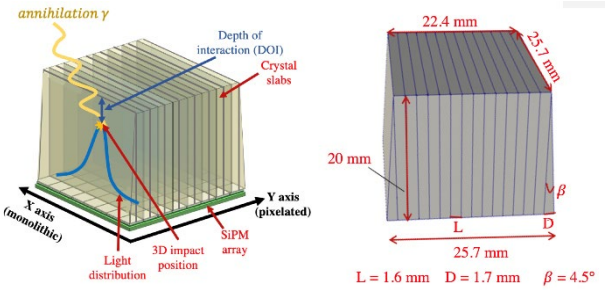

Figure 1: Left. Schematic representation of a photon impact in the 1×16 slab-shaped array. The scheme visually shows the DOI coordinate as well as the light distribution profile of the event, which is constrained to one slab. Right. Detailed drawing of the LYSO scintillation array used for the 4D-PET construction. The dimensions of the block are depicted.

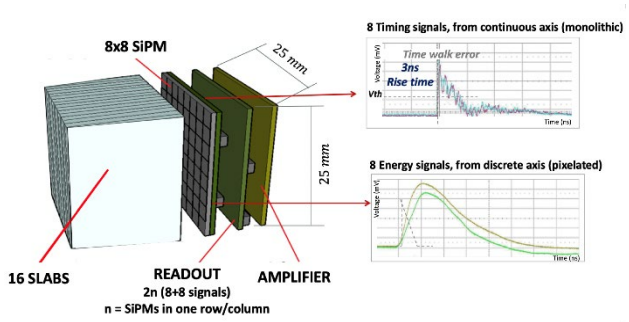

Figure 2: Left. Illustration of the detector including the scintillator array, the 8×8 SiPM matrix, the reduction readout board and, the amplifier. Right-top. Timing information (8 signals) as the sum of the SiPMs charge in the columns along with the monolithic axis; Right-bottom. Energy information (8 signals) as the sum of the SiPMs charge in the rows along with the pixelated axis. This axis gives a slower signal with good linearity and the necessary information to provide the x position along the slab. The profile shown with dash lines represents the timing signal for comparison purposes.

Regarding the detector readout chain, preliminary custom electronics have been implemented to reduce the 8×8 SiPM signals to only 8+8 without impacting spatial and timing performance but, relaxing electronic complexity and cost (Figure 2-left) [24]. The electronics scheme consists of the analogic summation of the 8 SiPMs in each row (two slab) to provide fast and sharp signals for precise timing measurements (Figure 2-right, top). These 8 temporal signals will be also used for the estimation of the photon impact along the x coordinate (discrete information, pixelated-like behaviour). Additionally, a fast amplifier, with low input impedance, is electrically coupled to the timing signal. With this, a low-impedance path is created for fast transition signals, which reduces the total parasitic capacitance of the paralleled sensor arrangement improving the time response of the detector block. Similarly, the 8 row projections of the SiPMs are used for the estimation of the photon impact position coordinate along the y axis (continuous information, monolithic-like behaviour) as well as the energy of the event. Note that, the energy signals correspond to the attenuated temporal signals for each two slabs (Figure 2-right, bottom). Finally, the output signals are connected to a high-speed analogic specific integrated circuit (ASIC), the TOFPET2 from PETsys [25].

Experimental evaluation

For experimental validation, two of the previously described detector elements have been used to acquire data in coincidence mode by placing a ^{22}Na source in between the two detectors (see Figure 3-left). The detectors were separated ~50 mm (front face to front face) and located inside a black box for light shielding and, air cooling was used to keep the temperature in the range of 30-32 °C.

To find the optimal measurement conditions, the following parameters have been varied and evaluated: (i) the impedance of the reduction readout board; (ii) the ASIC front-end input stage impedance (*feib*: 59 (28 Ω) and 61 (42 Ω)) and; (iii) the ASIC integrator gain (*att*: 0 (2.5 gain) and 4 (3.65 gain)). Table 1 summarizes the specification of each configuration.

Additionally, the TOFPET2 threshold levels and the SiPMs overvoltage (*SiPMov*) were swept in a wide range. Note that the TOFPET2 ASIC has three different threshold levels named Th_1, Th_2 and Th_E. Th_1 is a low threshold level and is used for the timing branch, Th_2 is used for rejecting dark counts thus, avoiding dead-time

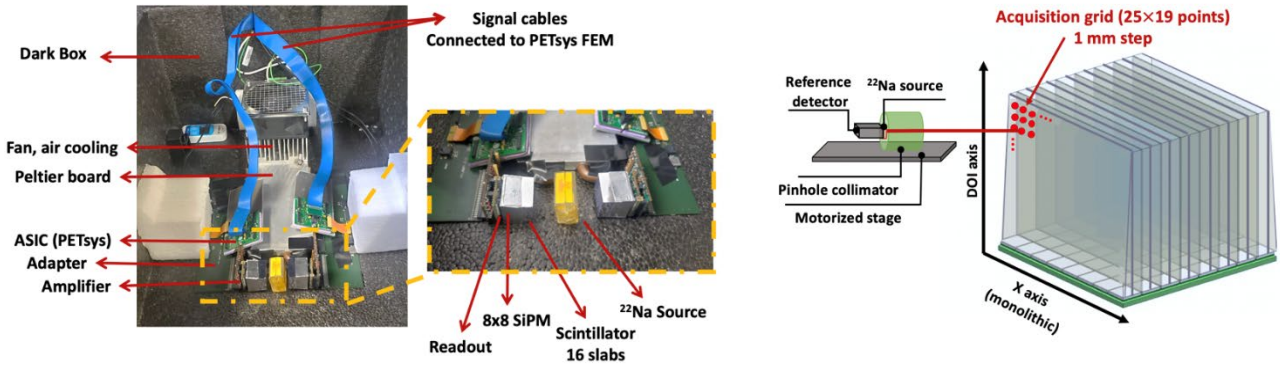

Figure 3: Left, Photo of the experimental setup used for the evaluation of the 4D-PET detectors. The photo shows the two detectors working in coincidences and the ^{22}Na source placed in between them (see yellow zoomed box). The electronic chain and the air-cooling system are also shown. Right, drawing showing the x-DOI acquisitions.

Configuration	Readout impedance (Ω)	ASIC integrator gain	Front-end input stage impedance (Ω)
1	1	0 (2.5 gain)	59 (28 Ω)
2	1	4 (3.65 gain)	59 (28 Ω)
3	1	0 (2.5 gain)	61 (42 Ω)
4	1	4 (3.65 gain)	61 (42 Ω)
5	2	0 (2.5 gain)	59 (28 Ω)
6	2	4 (3.65 gain)	59 (28 Ω)
7	2	0 (2.5 gain)	61 (42 Ω)
8	2	4 (3.65 gain)	61 (42 Ω)

Table 1: Specifications of the 8 different tested configurations for the 4D-PET detectors. Note that for each one of these configurations 72 different threshold and SiPMOV combinations were evaluated.

and, Th_E is a high threshold level used in the energy branch for event validation. These thresholds have been evaluated for the experiments with values of Th_1 = [10, 15, 20], Th_2 = [15, 20], and Th_E = [5, 10, 15, 20]. These thresholds are configurated in ASIC (digital-to-analog converted) DAC counts.

Regarding the *SiPMov*, values of = [3.5, 4.0, 4.5] V were also tested. The combination of these values yields to a total of 72 different cases for each configuration. Each acquisition lasted 60s, and six measurement trials were performed to provide the standard deviation of the results.

After finding the optimal measurement condition for the detectors, a fine-tuning of the threshold levels and *SiPMov* was performed for the configuration yielding the best results. This was configuration 7 (2Ω readout, *att* = 4, *feib* = 59) as explained in the next section. Therefore, values of Th_1 = [7, 10], Th_2 = [15, 20], and Th_E = [10, 12, 15] and, *SiPMov* of = [4.3, 4.5, 4.7, 4.9] V were evaluated (48 more configurations). Each acquisition lasted 120 s.

Acquired data was analysed using a custom-coded Python 3.0 script [36]. For timing analysis, the CTR of the detectors was calculated as the Full-Width-at-Half-Maximum (FWHM) of the temporal difference of the photons detected in the two coincident modules. Note that, only those events falling within the Full-Width-at-Tenth-Maximum (FWTM) of the photopeak were considered. For assessing the energy performance, energy spectra were used to estimate the energy resolution as the ratio between the FWHM and the 511 keV channel of the photopeak.

Regarding spatial resolution, flood maps have been used to visually determine the resolvability of the slabs, i.e. y-resolution (transaxial). For the evaluation of the x- (along the monolithic axis) and DOI-resolutions, acquisitions were performed by displacing the ^{22}Na source (collimated with a pinhole of 2 mm) across the crystal x-DOI surface. In this case, a reference detector consisting on a LYSO pixel of 3.0×3.0×10.0 mm^3 was used for acquiring coincidence data. Two step motors were employed to move the collimated source + reference detector in steps of 1 mm creating a grid of 25×19 positions (see Figure 3-right). For the x-DOI data analysis, a neural network (NN) algorithm was implemented [37]. The NN consisted on two multilayer perceptron architectures that contain two hidden layers of 100 nodes each. Acquired data was split in three data sets, namely: train, evaluation and test, each one containing 50%, 5% and 45% of the data, respectively. For training, the Adam optimizer using the rectifier linear activation function (RELU) and the mean average error (MAE) function were used. As input for the NN the 8+8 output signals provided by the reduction readout were introduced. The MAE and FWHM were calculated to provide the x- and DOI- resolution.

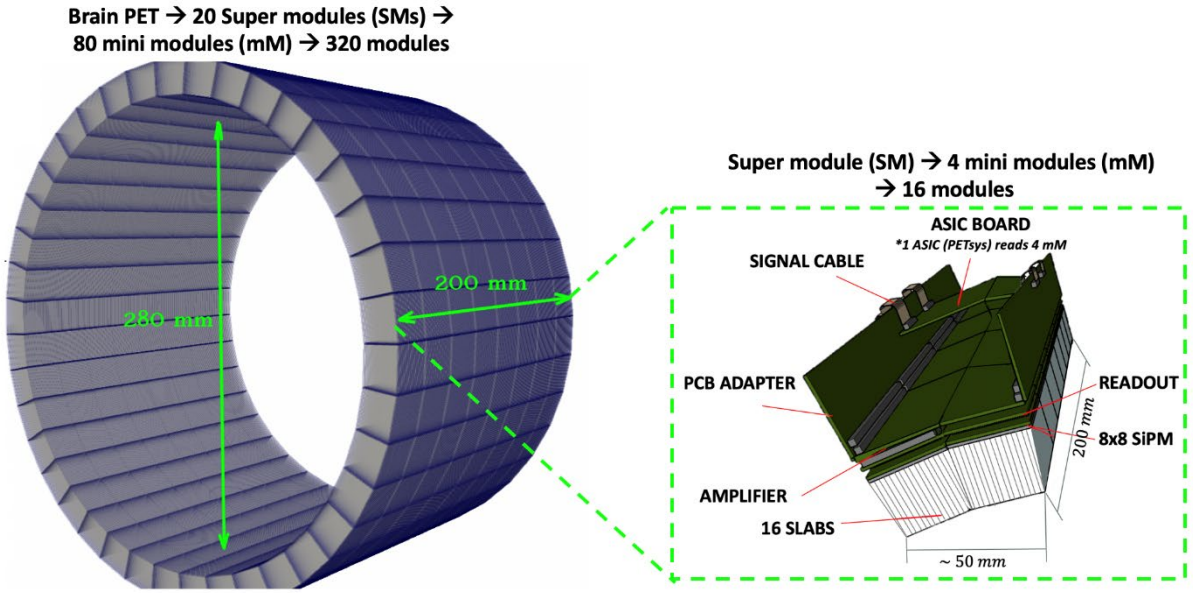

Figure 4: 4D-PET geometry showing the 320 detectors arranged in 8 rings. The green zoomed box (right) depicts the conceptual description of a Super Module (SM) which is composed of 16 modules (256 signals/SM).

Simulation studies

The 4D-PET prototype is composed of 320 of the previously described detector elements. To cover almost completely all the areas of the human brain, the detectors are arranged in 8 rings (40 detectors/ring) covering an axial length of 200 mm and a diameter of 280 mm. Figure 4 shows the 4D-PET geometry and the conceptual description of a Super Module (SM) which is composed of 16 modules.

Roughly, the spatial resolution (FWHM) of the 4D-brain can be approximated by the slab thickness (1.6 mm) as shown in the result section. Considering this resolution and, to infer the imaging performance of the final 4D-PET prototype, simulations of the system have been carried out using the GATE/GEANT Monte Carlo (MC) platform [38]. To provide realistic simulations of the 4D-PET, the measured performance of a pair of slab-shaped crystals attached to SiPMs have been used for the model. Given this input, the absolute sensitivity of scanner has been estimated following the NEMA 2008 protocol [39]. To do so, 0.3 mm ^{22}Na sources were simulated inside a plexiglass cube with dimensions of 10×10×10 mm^3. The sources were measured in steps of 15 mm across the entire FOV of the system [-90 to 90 mm].

To estimate the image quality, a Derenzo phantom was simulated at the centre and at 10 mm off-centre of the FOV. Also, the Hoffman brain phantom has been simulated and reconstructed with and without incl-uding TOF information. In this later case, a CTR of 205 ps have been used since, based on the simulations and previous experiments we hypothesize this will be achieved with the next generation of the readout electronics (currently under fabrication). For both the Derenzo and Hoffman phantom simulations, back-to-back gammas were used. The images were reconstructed using a list mode algorithm (0.5 mm^3 voxel size, 10 iterations and no data correction applied) [40]. Additionally, the 4D-PET Hoffman image has been verified with the one obtained with simulations of the Siemens Biograph MCT and Siemens Biograph Vision under the same conditions [41]. Also, the provided Hoffman real image in [42] by Siemens system is shown as a reference.

Results

Experimental results

The CTR, energy performance and slab identification have been evaluated for each one of the configurations described in Table 1. Table 2, summarizes the energy resolution (ER) for each module (M_1 and M_2) and, the CTR for the best threshold combination and *SiPMov*, for each one of the configurations described in Table 1.

Figure 5- left and right, depicts the flood map and energy spectra for detector M_1, and the corresponding CTR histogram, respectively, obtained for

Conf. (r_att_feib)	ER, M_1 (%)	ER, M_2 (%)	CTR (ps)	$SIPM_{OV}$	Threshold (Th_1_Th_2_Th_E)
1: (1_0_59)	15.1±1.3	14.5±1.5	416±5	4.5	10_20_5
2: (1_4_59)	11.3±1.6	11.4±1.9	442±5	4.5	10_20_5
3: (1_0_61)	15.4±2.1	14.5±1.9	461±7	4.0	10_15_10
4: (1_4_61)	11.7±1.8	11.5±2.4	433±9	4.5	10_20_15
5: (2_0_59)	13.6±1.1	12.7±1.7	406±5	4.5	10_20_15
6: (2_0_61)	14.2±2.0	12.8±1.4	402±7	4.5	15_20_10
7: (2_4_59)	10.3±1.8	10.2±1.5	359±7	4.7	7_20_10
8: (2_4_61)	12.1±1.3	12.2±1.4	483±8	4.0	10_20_10

Table 2: Flood map quality, energy resolution (ER) for each module and, CTR results, measured for the best threshold (in DAC units) combination and *$SiPM_{OV}$* for the configurations shown in Table 1.

the best parameter configuration which resulted to be a readout impendence of 2Ω, an ASIC front-end input stage impedance *feib* of 59 (28 Ω), an ASIC integrator gain *att* of 4 (3.65 gain), a threshold configuration of (Th_1, Th_2, Th_E) = (7,20,10) and *$SIPM_{OV}$* of 4.7 V. The flood map shows the line profile measured for the slabs to demonstrate its clear identification thus, a resolution in the pixelated axis <1.6 mm is achieved.

Regarding x-resolution and DOI resolution, the 4-D PET detector achieved average x-MAE and x-FWHM values of 1.2±0.3 mm and 2.7±0.5 mm, respectively; and average DOI-MAE and DOI-FWHM values of 1.9±0.7 mm and 3.4±1.1 mm, respectively. An energy filter of 30% around the photopeak was applied during data analysis.

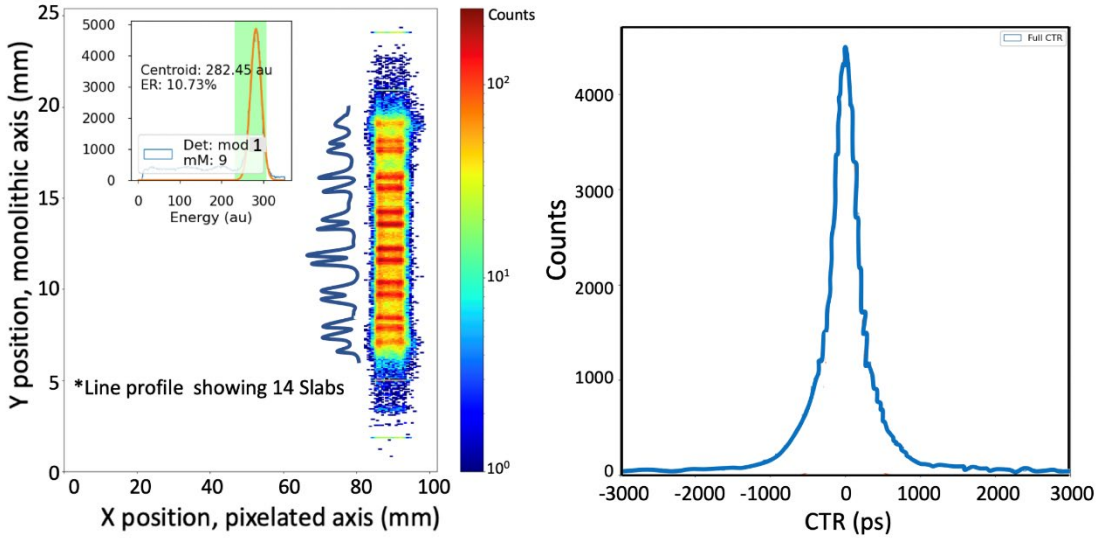

Figure 5: Flood map including the energy spectra of M_1 (left), and measured CTR histogram (right) for the best parameter configuration obtained during the fine-tuning studies.

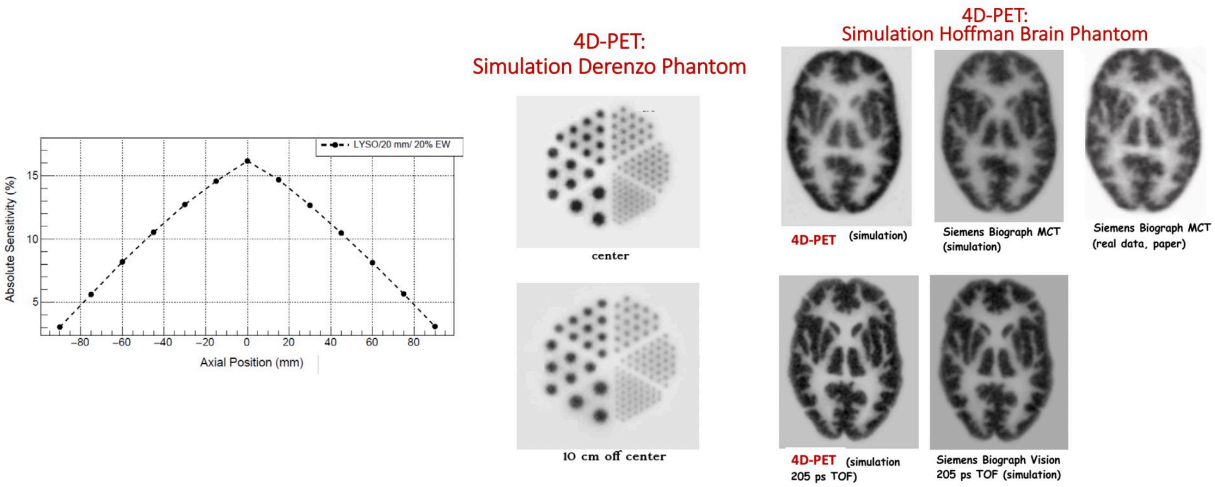

Figure 6: Left, estimated absolute sensitivity of the 4D-PET system. Centre, reconstructed images of the Derenzo phantom when simulated at the centre (top) and at 10 cm off-centre (bottom) of the 4D-PET scanner FOV. Right, reconstructed images of the Hoffman Brain phantom with (top) and without (bottom) including TOF information. The images are compared with the ones obtained with the state-of-the-art Siemens Biograph MCT, extracted from reference [41].

Simulation results

The estimated sensitivity and the list mode reconstruction images corresponding to the simulation phantoms are shown in this section.

Figure 6-left shows the estimated absolute sensitivity of the system after applying a 20% energy window around the photopeak. The sensitivity at the centre of the FOV was found to be 16.2%, this value decreases to 3.1% at the edges of the FOV (90 mm off-centre).

Figure 6-centre depicts the reconstructed images of the Derenzo phantom simulated at the centre (top) and at 10 cm off-centre (bottom) of the 4D-PET scanner FOV. As can be appreciated in the images, all rods are clearly distinguished, even the smallest ones of 1.2 mm. On the right side of Figure 6, the reconstructed images of the Hoffman Brain phantom are depicted with (top) and without (bottom) including TOF information. Both cases report an image quality that allows for the visualization of the small structures of the brain. Finally, the Hoffman real data reference image is similar to those obtained in the performed simulations, validating the results obtained in these simulations [40-43].

Future work

At this time and based on the experimental results obtained in the laboratory, the first 4D-PET prototype is being built. The 4D-PET prototype is composed of 320 of the previously described detector elements, each one providing 8+8 output signals. This implies a total of 5120 signals (8+8 signals/detector × 40 detectors/ring × 8 rings = 5120 signals).

Regarding the electronics chain of the 4D-PET, the system has been designed as follows: 160 custom-designed amplifier printed circuit boards (PCB) with dimensions of 48.4×24.2 mm² are used, each one allocates two modules (32 signals); then, four of these amplifier boards (8 modules, 128 signals) are connected to an adapter PCB with dimensions of 205×45 mm² thus, the 4D-PET system comprises a total of 40 PCB adapters. The PCB adapter is used for transferring the analogic output signals provided by the reduction readout board to the TOFPET2 ASIC. Each adapter is connected to 2 TOFPET2 ASICs (each ASIC allows 64 signals: 4 modules), thus, a total of 80 ASICs are used. Next, the ASICs are connected to 20 FEMs (16 modules/FEM) which are responsible of digitalizing the analogic signals and provide the timestamp and energy of the event. These FEMs are connected also to two FEB/Ds: one of 4k (4096 channels) and one of 1k (1024 channels). The FEB/Ds are connected to the clock trigger board for event ordering and threshold validation. Finally, the data is transferred to the PC for analysis. Note that, the quantity and size of the elements has been chosen to optimize the number of electronical components required. To do so we have tried to match as much as possible the number of readout output signals with the number of ASICs. Moreover, for the custom-designed PCB boards small foot-print components have been used to reduce the gaps between

detectors and maximize the system sensitivity. Table 3 summarizes the number of components used in the 4D-PET design.

Element	Quantity	Notes
Slabs	5120	Polished surface and ESR wrapping
1×16 Scintillation array	320	Trapezoidal shape
SiPMs	20480	S13 Hamamatsu
8×8 SiPM matrix	320	64 output signals each
Reduction Readout	320	Allows to reduce from 64 to 16 signals/SiPM (4:1)
Signals	5120	Without reduction would be 20480
Amplifier	180	1 amplifier allocated 2 modules
PCB Adapter	40	1 adapter allocated 4 amplifiers (8 modules)
PETsys ASIC	80	2 ASICs/adapter. Each one allows 64 input signals.
FEM	20	Each FEM allocates 16 modules (256 signals)
FEB/D	2	One of 4k (4096 ch) and one of 1k (1024 ch)
Clock/trigger board	1	Triggers the signals

Table 3: Quantity and specification of elements used in the design of the 4D-PET.

The power consumption of the 4D-PET system is calculated to be 120 W, a total of four voltage suppliers are used to feed the detectors. Water cooling cold plates have been selected to dissipate the heat generated by the detectors as Figure 7 shows.

Figure 7 depicts the first photos of the real 4D-PET, which shows the scanner structure with the 320 scintillation elements already inserted and, the first mechanical design of the holder which already includes the cold plates for the cooling system.

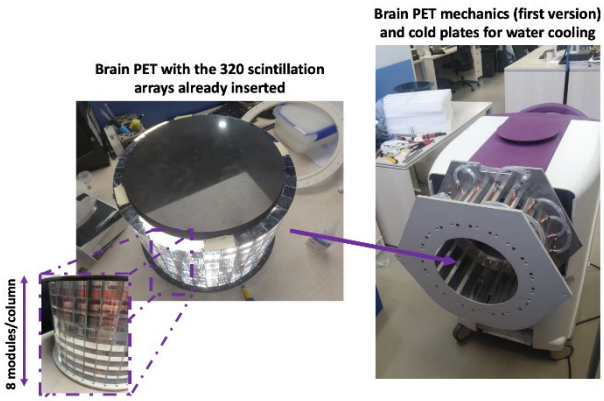

Figure 7: First photos of the 4D-PET showing the scanner bore with the 320 scintillation elements (purple box) and, the first mechanical design of the system holder which already includes the cold plates for the cooling system.

Discussion

The present manuscript describes the novel design of the 4D-PET scanner which is an organ-specific imaging system dedicated to the study of the human brain and its disorders. As estimated through calculations based on MC simulations of the scanner, the 4D-PET is expected to provide high effective sensitivity, more than 10 times better than current WB-PETs on the market. Figure 8 shows a comparison of the absolute sensitivity (values from [43-49], and references therein) of commercial and, under development PET scanners. The absolute sensitivity of the 4D-PET (16.6% at the centre of the FOV) is beyond current state-of-the-art WB-PET scanners.

The slab configuration is key to ensure good spatial resolution in the trans-axial plane(s) which is estimated to be ~ 1 mm in the reconstructed imaged - approximated the slab thickness (1.6 mm)/√2-, while providing a below 300 ps TOF information. Actually, the measurements performed with two modules achieves a 3D spatial resolution - <1.6 mm in the transaxial plane and ~2.7 mm in the axial plane. For the x- and DOI- resolution, a NN was implemented showing a good agreement with previous studies that were carried out using similar blocks [19] (<3.5 mm). Also, the implemented detector incorporates a novel reduction readout PCB that has demonstrated to be able of reducing the number of sign–

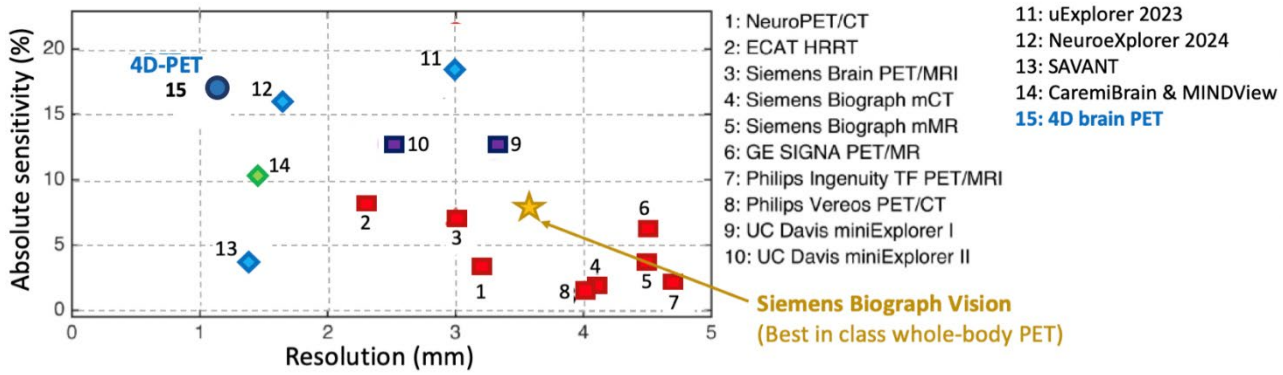

Figure 8: Comparison of the absolute sensitivity (extracted from [43-49], and references therein) of commercial and, under development PET scanners. The absolute sensitivity of the 4D-PET (16.6% at the centre of the FOV) is beyond current state-of-the-art scanners WB-PET. In the plot we are using red, purple, blue and green colors to represent PET systems that are commercial, for research, under development and, based on monolithic scintillators, respectively.

–als in a ratio of 4:1 - alleviating system complexity and cost- without impacting performance [24]. In view of these results and combined with the expected value in sensitivity estimated by simulations, 4D-PET could allow differentiating even small changes in activity, neurotransmitter production and neurochemistry in small brain regions, which is currently beyond the capabilities of any WB-PET device. Furthermore, by significantly reducing partial volume effect using TOF information and eliminating the need for its correction, unprecedented dynamic accuracy could at last be possible in assessing key areas such as prefrontal cortex, limbic lobe, substantia nigra and nuclei from the thalamus, as well as refining the synaptic density [50]. As shown in Figure 6, the reconstructed Hoffman brain phantom images show an image quality comparable to the one provided by the state-of-the-art Siemens Biograph MCT [41] but at a much lower cost thus, making the 4D-PET system accessible to more hospital facilities.

Conclusion

Promising detector performance has been achieved using a semi-monolithic based gamma detector with a reduced number of signals. The 4D-PET detector design tries to go beyond current PET technology and is expected to come up with new applications for PET in biomedical research. Moreover, the detector is suitable for systems requiring large number of detectors (i.e., signals) and brings us closer to the goal outlined at the beginning of this project: boosting sensitivity by building practical and transferrable brain PET systems.

The estimated sensitivity in 4D-PET system can be considered as a cornerstone for next generation PET devices, as it can be used at both high and very low tracer concentrations, minimizing data noise, validating faster and more effectively new tracer pharmacokinetics, pharmacodynamics and (brain/CNS) biodistribution, and specially, assessing dynamic changes i.e., of neurotransmitters such as serotonin and dopamine [51].

Acknowledgements

This project has received funding from the European Research Council (ERC) under the European Union's Horizon 2020 research and innovation program (Grant Agreement No. 695536). This work was supported in part by the Spanish Government Grants Generalitat Valenciana, APOSTD/2019/086 and APOSTD/2020/139. We thank financial support from Generalitat Valenciana through the program Equipamiento e Infraestructuras FEDER 2021-22 IDIFEDER/2021/004.

References

[1] Phelps ME. Positron emission tomography provides molecular imaging of biological processes. Proc Natl Acad Sci USA. 2000;97:9226–9233.

[2] Moliner L, Rodríguez-Álvarez MJ, Catret JV, González A, Ilisie V, Benlloch JM, Performance Evaluation of CareMiBrain dedicated brain PET and Comparison with the whole-body and dedicated brain PET systems. Sci Rep. 2019 Oct 29;9(1):15484. doi: 10.1038/s41598-019-51898-z

[3] González AJ, Sánchez F, Benlloch JM. Organ-dedicated molecular imaging systems. IEEE Trans. Radiat. Plasma Med. Sci., vol. 2, no. 5, pp. 388–403, Sep. 2018.

[4] Hsu DFC, Freese DL, Reynolds PD, Innes DR, Levin CS. Design and performance of a 1 mm3 resolution clinical PET system comprising 3-D position sensitive scintillation detectors. IEEE Trans. Med. Imag., vol. 37, no. 4, pp. 1058–1066, Apr. 2018,

[5] Miyaoka RS, Hunter WCJ, DeWitt DQ, Pierce L. Performance characteristics for a low cost, dual sided, position sensitive sparse sensor (DS-PS3) PET detector with depth of interaction positioning. Proc. IEEE Nucl. Sci. Symp. Med. Imag. Conf.

[6] Benlloch JM, Gonzalez AJ, Pani R, Preziosi E, Jackson C, Murphy J, BArbera J, Correcher C, et al. The MINDVIEW project: First results. Eur. Psychiatry, vol. 50, pp. 21–27, Apr. 2018.

[7] Marti-Climent JM, Prieto E, Moran V, Sancho L, Rodriguez-Fraile M, Arbizu J, Garcia-Velloso MJ, Ritcher JA. Effective dose estimation for oncological and neurological PET/CT procedures JNMMI Research. vol. 7(37), April 2017.

[8] Brownell GL, Sweet WH. Localization of brain tumors with positron emitters. Nucleonics, vol. 157, no. 14, pp. 1183–1188, Apr 1955.

[9] Zaidi H, Montandon ML. The New Challenges of Brain PET Imaging Technology. Curr. Med. Imaging. vol. 2(1), pp. 3-13, 2006.

[10] Conti M, Bendriem B. The new opportunities for high time resolution clinical TOF PET. Clinic. Trans. Imaging. vol. 7, pp. 139-147, 2019.

[11] Gonzalez-Montoro A, Aguilar A, Cañizares G, Conde P, Hernandez L, et al. Performance study of a large monolithic LYSO PET detector with accurate photon DOI using retroreflector layers. IEEE Trans. Radiat. Plasma Med. Sci., vol. 1, no. 3, pp. 229–237, May 2017.

[12] LaBella A, Petersen E, Cao X, Zeng X, Zhao W, Goldan A. 36-to-1 multiplexing with Prism-PET for high resolution TOF-DOI PET. J Nucl Med. 2021; 62(suppl 1):38.

[13] Majewski S. Perspectives of brain imaging with PET systems. Bio-Algorithms and Med-Systems 17:269–291, 2021.

[14] Gonzalez-Montoro A, Ullah MN, Levin CS. Advances in detector instrumentation for PET. J. Nucl. Med. vol. 63(8), pp. 1138-1144, Aug 2022.

[15] Gonzalez-Montoro A, Pourashraf S, Lee MS, Cates JW, Levin CS. Study of optical reflectors for a 100ps coincidence time resolution TOF-PET detector design. Biomed Phys Eng Express. 2021;7:65008.

[16] Bizarri G. Scintillation mechanisms of inorganic materials: from crystal characteristics to scintillation properties. J Cryst Growth. 2010;312:1213–1215.

[17] Zhang X, Wang X, Ren N, Kuang Z, Deng X, Fu X, et al., Performance of a SiPM based semi-monolithic scintillator PET detector. Phys. Med. Biol., vol. 62, no. 19, pp. 7889–7904, Sep. 2017.

[18] Cucarella N, Lamprou E, Valladares C, Benlloch JM, Gonzalez AJ. Timing evaluation of a PET detector block based on semi-monolithic LYSO crystals. Med. Phys. vol 48(12), pp. 8010-8023, Dec 2021.

[19] Schaart DR, Charbon E, Frach T, Schulz V. Advances in digital SiPMs and their application in biomedical imaging. Nucl Instrum Methods Phys Res A. 2016;809: 31–52.

[20] Gundacker S. Heering A. The silicon photomultiplier: fundamentals and applications of a modern solid-state photon detector. Phys. Med. Biol. 65 17TR01, 2020.

[21] Lecoq P, Gundacker S. SiPM applications in positron emission tomography: toward ultimate PET time-of-flight resolution. The European Physical Journal Plus. vol. 136, aticle number: 292, 2021.

[22] Berg E, Cherry SR. Innovations in instrumentation for positron emission tomography. Semin Nucl Med. 2018;48:311–331.

[23] Alessio AM, Stearns CW, Tong S, Ross SG, Kohlmyer S, Ganin A, Kinahan PE. Application and Evaluation of a Measured Spatially Variant System Model for PET Image Reconstruction. IEEE Trans. Med. Imaging. vol. 29(3), pp. 938-949, March 2010.

[24] Benlloch JM, Pavon N, Barbera J, Gonzalez AJ. Topología de red de lectura para dispositivos de tomografía de emisión de positrones con tiempo de vuelo. P202130959 - 12/10/2021. https://aplicat.upv.es/exploraupv/ficha-tecnologia/patente_software/37411

[25] Bugalho R, Di Francesco A, Ferramacho L, Leong C, Niknejad T, Oliveira L, Rolo M, Silva JC, Silveira M. Experimental characterization of the TOFPET2 ASIC. JINST 14 P03029, 2019.

[26] Herbert G, Duffau H. Revisiting the Functional Anatomy of the Human Brain: Toward a Meta-Networking Theory of Cerebral Functions. Physiolo. Reviews. vol. 100(3), pp. 1181-1228, 2020.

[27] Moskal P, Stepien Ewa. Prospects and Clinical Perspectives of Total-Body PET Imaging Using Plastic Scintillators. PET Clin. 5(4):439-452, 2020.

[28] Moskal P, Kowalski P, Shopa R Y, et al. Simulating NEMA characteristics of the modular total-body J-PET scanner—an economic total-body PET from plastic scintillators. Phys. Med. Biol. 67 175015, 2021.

[29] Pawel P, Dulski K, Chug N, et al., Positronium imaging with the novel multiphoton PET scanner. Sci Adv; 7(42), 2021.

[30] Levin CS. Promising Detector Concepts to Advance Coincidence Time Resolution for Time-of-Flight Positron Emission Tomography. Acta. Phys. Polon. A 142:422, 2022.

[31] Gonzalez-Montoro A, Gonzalez AJ, Pourashraf S, et al. Evolution of PET detectors and event positioning algorithms using monolithic scintillation crystals. IEEE Trans Radiat Plasma Med Sci; 5:282–305, 2021.

[32] Müller F, Naunheim S, Kuhl Y, Schug D, Solf T, Schulz V. A Semi-Monolithic Detector providing intrinsic DOI-encoding and sub-200 ps CRT TOF-Capabilities for Clinical PET Applications. Inst. Det; Med. Phys. arXiv:2203.02535, 2022.

[33] 3MTM Enhanced Specular Reflector Films (ESR). Technical data, 2020. https://multimedia.3m.com/mws/media/1245089O/3m-enhanced-specular-reflector-films-3m-esr-tech-data-sheet.pdf

[34] BC-630 Silicone Optical Grease, Saint Gobain datasheet. https://www.crystals.saint-gobain.com/radiation-detection-scintillators/assembly-materials

[35] MPPC® (Multi-pixel photon counter), S13360 Series, Hamamatsu Photonics. https://www.hamamatsu.com

[36] Python 3.0 user guide. https://www.python.org/doc/

[37] Freire M, Echegoyen S, Gonzalez-Montoro A, Sanchez F, Gonzalez AJ. Performance Evaluation of Side-by-Side Optically Coupled Monolithic LYSO Crystals. Med. Phys. vol. 49(8), pp. 5616-5626, 2022.

[38] Jan S, Santin G, Strul D, Steaelens S, Assie K, Autret D, Avner S, Barbier R, et al. GATE: a simulation toolkit for PET and SPECT. Phys Med Biol. vol. 49(19), pp. 4543-61, 7 Oct 2004.

[39] NEMA NU 4-2008. Performance measurements of Small Animal Positron Emission Tomographs. (Association, National Electrical Manufacturers, 2008).

[40] Moliner L, Correcher C, Gonzalez AJ, Conde P, Hernandez L, Orero A, Rodriguez-Alvarez MJ, Sanchez F, Soriano A, Vidal LF, Benlloch JM. Implementation and analysis of list mode algorithm using tubes of response on a dedicated brain and breast PET. Nucl Instrum Methods Phys Res A. vol 702, pp. 129-132. 2013.

[41] Herzog H, Tellmann L, Marx B, Rota Kops E, Scheins J, Weirich C, Shah NJ. Performance Tests and Preliminary Results of the 3TMR-BrainPET Scanner Installed at the Forschungszentrum Jülich. WC 2009, IFMBE Proceedings 25/II, pp. 677–680, 2009.

[42] Van Vonderen K, Leonard S, Linscheid L, Gruchot M, Dillehay G. Image quality assessment of Hoffman brain phantom scans performed on a next generation and previous generation PET/CT scanners. Image quality assessment of Hoffman brain phantom scans performed on a next generation and previous generation PET/CT scanners. J. Nucl. Med. vol. 60(1) 2052. May 2019.

[43] Vandenberghe S, Moskal P, Karp JS. State of the art in total body PET. EJNMMI Phys. 2020;7:35.

[44] Spencer BA, Berg E, Schmall JP, Omidvari N, Leung EK, et al. Performance Evaluation of the uEXPLORER Total-Body PET/CT Scanner Based on NEMA NU 2-2018 with Additional Tests to Characterize PET Scanners with a Long Axial Field of View. J. Nucl. Med. vol. 1(62), pp. 861-870. Jun 2021.

[45] Karlberg AM, Sæther O, Eikenes L, Goa PE. Quantitative comparison of PET performance-Siemens Biograph mCT and mMR. EJNMMI Phys. vol. 3(1): 5. Dec 2016.

[46] Surti S, Kuhn A, Werner ME, Perkins AE, Kolthammer J, Karp JS. Performance of Philips Gemini TF PET/CT scanner with special consideration for its time-of-flight imaging capabilities. J. Nucl. Med. vol. 48(3), pp. 471-80. Mar 2007.

[47] Caribe PRRV, Koole M, D'asseler Y, Deller TW, Van Laere K, Vandenberghe S. NEMA NU 2–2007 performance characteristics of GE Signa integrated PET/MR for different PET isotopes. EJNMMI Physics. vol. 6(11). July 2019.

[48] Gaudin E, Toussaint M, Thibaudeau C, Fontaine R, Normandin M, Petibon Y, Ouyang J, El Fakhri G, Lecomte R. Simulation Studies of the SAVANT High Resolution Dedicated Brain PET Scanner Using Individually Coupled APD Detectors and DOI Encoding. J. Nucl. Med. vol. 60(1), pp. 531. May 2019.

[49] Gonzalez AJ, Gonazlez-Montoro A, Aguilar A, et al., "Initial results of the MINDView PET insert inside the 3T mMR. IEEE Trans. Radiat. Plasma Med. Sci., vol. 3, no. 3, pp. 343–351, May 2019.

[50] Ceccarini J, Liu H, Van Laere K, Morris ED, Sander CY. Methods for Quantifying Neurotransmitter Dynamics in the Living Brain With PET Imaging. Front. Physiol., 10.3389. July 2020.

[51] Yang J, Hu C, Guo N, Dutta J, Vaina LM, Johnson KA, Sepulcre J, El Fakhri G, Li Q. Partial volume correction for PET quantification and its impact on brain network in Alzheimer's disease. Scientific Reports. vol. 7, article number: 13035. Oct 2017.